Research Square

Preprints are preliminary reports that have not undergone peer review.
They should not be considered conclusive, used to inform clinical practice,
or referenced by the media as validated information.

Negative Differential Resistance Devices Using Edge Modified MgO Nanoribbons: A DFT Investigation

Javvadi Sambasivarao
VIT-AP University
Aruru Sai Kumar
saikumar.a@vitap.ac.in
VIT-AP University

Article

Keywords:

Posted Date: August 19th, 2026

DOI: https://doi.org/10.21203/rs.3.rs-10605687/v1

License: This work is licensed under a Creative Commons Attribution 4.0 International License.
Read Full License

Additional Declarations: No competing interests reported.

Negative Differential Resistance Devices Using Edge Modified MgO Nanoribbons: A DFT Investigation

Javvadi Sambasivarao[1] **and Aruru Sai Kumar**[2,*]

[1,2]School of Electronics Engineering, VIT-AP University, Near AP secretariat, Amaravathi, Andhra Pradesh 522241
[*]Corresponding Author: saikumar.a@vitap.ac.in

ABSTRACT

MgO nanoribbons (MgONRs) are analyzed using the first principles approach using density functional theory (DFT) for potential nanoelectronic applications. Chemically edge modified MgONRs are investigated for their electrical characteristics. The structural investigations reveal the nanoribbons are thermodynamically stable and chlorination at the edges relatively reduces the stability of the structures. Bandstructures calculations reveal the bare MgONRs and chlorine passivated MgONRs are all metallic structures. Further, the two-probe methodology is deployed for the voltage-current ($V-I$) characteristics. The chlorine passivation is found to significantly enhance the current magnitude and an interesting negative differential resistance phenomenon is noticed in all the chlorine passivated structures. MgONRs having chlorine passivation at Mg-edge (Cl-MgO-B) has relatively higher peak-to-valley current ratio (PVCR). The observed results shows that the chlorinated MgONRs have the potential to be deployed in future nanoelectronic steep switching devices, tunnel devices, oscillators etc.

Introduction

The oustanding achievements of semiconductor sector in performance and productivity was possible because of the downsizing of complimnetary metal oxide semiconductor (CMOS) devices. Conventionally, development of novel lithographic tools, key-size etching processess, phototresist materials, and masks have facilitated these advancements[1,2]. During the initial years of integrated circuit (IC) design, reduction in channel length and gate oxide thickness were the primary starategies. This led to the improved packaging density and performance[3]. However, as the downscaling of the transistors reached nanoscale dimensions, the IC performance is limited due to factors such as short channel effects (SCEs), unwanted tunnelling effects[4]. To continue the semiconductor advancements, various novel device architectures are designed including fin-field effect structures (FinFETs), silicon on insulator (SOI) FETs, gate all around (GAA) FETs etc., are developed to reduce the SCEs and to improve the gate channel controllability[5–7]. However, these devices are faced with several fundamental limitations which include large parasitic capacitance, achieving physical gate length at sub-nanometer dimensions[8]. In order to address the challenges with scaling the body of 3D semiconductor devices, 2D materials have gained intense interest in recent years[9].

Two dimensional (2D) structures are the nanomaterials with thickness about a few atomic layers and very high aspect ratios. These nanomaterials confine the carriers in single/few atom thin channel structure[9,10]. 2D semiconductor devices have shown significant contributions in nanotechnology applications over the past two decades owing to their excellent gate controllability, atomic thickness and efficient carrier transport properties[11]. The first 2D material graphene has attracted several researchers across the world due to its outstanding characteristics such as conductivity, high mobility, lower weight and higher structural rigidity etc. These properties of atomic layer thin graphene make it an ideal material for integration into semiconductor technology for a variety of applications. Despite its zero bandgap nature, the quasi-1D allotropes of graphene called graphene nanoribbons are extensively investigated for opening a bandgap.[12]. Following graphene, numerous other 2D materials like metal oxides, metal nitrides, transition metal dichalcogenides are being explored by researchers[13]. Because of the quantum confinement effects and the variation in crystal structures, these 2D variants show a diversified electronic and magnetic properties in comparison to their bulk forms.[14,15].

Among these 2D materials, MgO nanosheets are of particular interest due to their enivronment friendly nature, ability to absorb toxic heavy metals etc.[16]. Also, they are potential candidates in optical, nano-electronic, solar cells, and FETs applications. They are also promising candidates as unreactive substrates and catalysts.[17–19] MgO is a wide bandgap material which is often used in toxic waste factories, paints, remediation, catalysis, etc[20]. Due to their excellent characteristics, many scientists have started to explore MgO nanostructures including nanosheets, nanoribbons, nanowires etc.[19]. MgO nanosheets are experimentally realized with various methods such as epitaxial growth[21], hydrothermal method[22], and chemical vapor deposition[23]. Graphene-like hexagonal MgO nanosheets are found to be lesser stable structures compared to bulk rocksalt structure by just about 0.06 eV[24]. MgO 2D nanosheets with polar and non-polar structures are experimentally synthesized on

various substrates. MgO with planar hexagonal arrangement of Mg and O atoms is grown on silver and gold susbtartes[25,26]. Polar structures exhibit interesting electronic and magnetic characteristics. The quasi-1D allotropes MgO called MgO nanoribbons can be carved out MgO nanosheets with different edge patterns either zigzag or armchair[27]. Recently, zigzag MgO nanoribbons are explored for interconnect applications[28]. Additionally, the electronic characteristics of MgO nanoribbons are investigated under the influence of vacancies, dopants and passivation[29]. Furthermore, arsenic functionalization on MgO nanoribbons are also investigated for potential arsenic sensor design[30]. Negative differential resistance (NDR) refers to the mechanism where the device current reduces upon the potential applied across the device is increased. This intriguing property of the devices is used in various applications like resonant tunnel diodes (RTDs), oscillators, steep switching devices, etc[31]. Various other materials are explored for NDR characteristics in 2D material devices[32–36]. Among metal oxides ZnO nanoribbons are explored for NDR characteristics with chemical modifications such as selective passivation[37].

In view of this zigzag MgONRs are considered for the first principles investigations with chlorine passivation at Mg-edge (Cl-MgO-B), O-edge (B-MgO-Cl), and chlorine passivation at both edges (Cl-MgO-Cl). The considered nanoribbon structures are shown in Figure 1. The transport characteristics of the evaluated structures show a significant enhancement in current magnitude with NDR characteristics. It is observed that edge chlorination in the structures causes significant increase in current magnitude. B-MgO-B has relatively lower current magnitude compared to chlorinated structures which could be due to the edge interactions. Further, the NDR characteristics are analyzed with transmission spectrum analysis. The findings suggest that the MgONRs with chlorine passivation have huge potential in nanoelectric applications including steep switching devices, tunnel devices, oscillators etc.

The remaining contents of the manuscript contains models and methods in Computational Method section while Results and Discussion section focussess on extensive discussion of the obtained results. Finally the conclusion statements are presented in Conclusion section.

Computational Method

The electrical characteristics of the chlorine passivated MgONRs are investigated using density functional theory (DFT) alongside non-equilibrium Green's function (NEGF) formalism. For the computational simulations, QuantumWise ATK tool is used[38,39]. The MgONR nanoribbon structures are built with open boundary conditions in the Z-direction and confining the structures in X and Y directions. To avoid the periodic image interaction along X- and Y- directions, a sufficient vacuum padding space of 10 Å is used. The structures are intially relaxed until the interatomic forces are less than 0.01 eV with a tolerance of the order of 10^{-5} to obtain the lowest energy state. For relaxation a dense mesh cut-off energy of about 150 Ry is used[40]. For sampling of the Brillouin zone, a dense k-point sampling of $1 \times 1 \times 100$ is employed using Monkhorst-Pack scheme[40]. The exchange correlational effects in the structures are modelled using the generalized gradient approximation (GGA) within the framework of Perdew-Burke Ernzerohf functional (PBE)[41]. For the electronic interactions, double zeta polarized basis sets are used for the atoms. Using the binding energy (E_b) calculations, the relaxed structures are investigated for their structural stability. The E_b is calculated using the formalism shown in expression Eqn. 1[42].

$$E_b = \frac{1}{N_T}(E_T - pE_{Mg} - qE_O - rE_{Cl}) \tag{1}$$

In the expression in Eqn. 1, E_T refers to the total ground state energy of the structure while E_{Mg}, E_O, E_{Cl} represent the isolated energies of magnesium, oxygen and chlorine atoms, respectively. The atom counts are represented by p, q, and r in the same order. Additionally to investigate the transport characteristics, two probe model is deployed using the NEGF formalism. The two-probe model has two semi-infinite electrodes with a scattering region at the center. The Landauer-B*ü*ttiker formula used to evaluate the $V-I$ characteristics is shown in Eqn. 2. Using the formalism in Eqn. 1, the current is computed as shown[43],

$$I(V) = \frac{2e^2}{h}\int_{\mu_L}^{\mu_R} T(E,V)[F(E-\mu_L) - F(E-\mu_R)]dE \tag{2}$$

The transmission coefficient ($T(E,V)$) is evaluated using the expression in Eqn. 3. The Fermi energy levels of the left/right electrodes are denoted by $\mu_{(L/R)}$.

$$T(E,V) = T_r[\tau_R(E,V)G_C(E,V)\tau_L(E,V)G_C^+(E,V)] \tag{3}$$

where, the advanced/retarded Green's function is represented by $G_C^+(E,V)/G_C(E,V)$. The electrode coupling coefficients are denoted by $\tau_L(E,V)$ (left) and $\tau_R(E,V)$ (right).

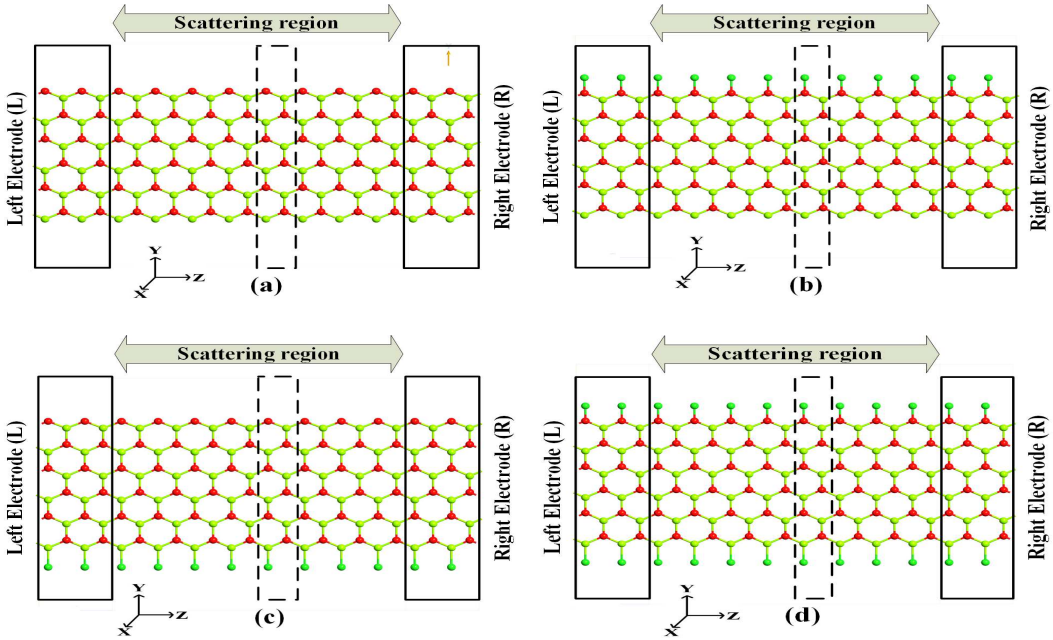


Figure 1. Two-probe structures of MgONRs (a) B-MgO-B, (b) B-MgO-Cl, (c) Cl-MgO-B and (d) Cl-MgO-Cl. Here, Cl, O, and Mg atoms are represented by dark green (at top/bottom), red, and light green (inside the bulk structure) spheres, respectively. The dashed rectangular box at center represents the unit cell.

Results and Discussion

A detailed discussion on the obtained simulation results of the MgONRs are presented in the following section. For simpler understanding, the following section is split into three subsequent sections each discussing, structural, electronic and transport properties accordingly.

Structural properties

The MgONR structures primarily undergo relaxation to obtain a ground state. The optimized bondlengths of the MgONRs are tabulated in Table 1. For the B-MgO-B structure, the edge Mg-O bondlengths are measured to be 1.88 Å and 1.86 Å along the edge with Mg-atoms and O-atoms, respectively. A slight contraction in the bondlength is noticed at the O-edge which could be the result of higher electronegativity of oxygen atoms at the O-edge. The bondlengths at the central area of the nanoribbon are noticed to be slightly elongated to 1.92 Å. The MgONRs are then investigated with chlorine passivation. For the nanoribbon with chlorine passivated at the O-edge, the chlorine atoms bond with O-atom with a bondlength of 1.88 Å. The edge MgO bondlengths are at 1.87 Å at O-edge and 1.90 Å at Mg-edge. The bondlength at the centre is contracted to 1.90 Å. A similar change is noticed for the nanoribbon with Cl passivation at the Mg-edge. For Cl-MgO-B, the central bondlength is measured at 1.90 Å while the Mg-O bondlengths at the O-edge and Mg-edge are found to be 1.90 Å and 1.86 Å. The Mg-Cl bondlenth at the edge is at 2.28 Å. Now for the nanoribbon with chlorine atoms passivated at both the edges (Cl-MgO-Cl), the Mg-O bondlength at Mg edge is 1.90 Å and at O-edge it is found to be 1.88 Å. The Mg-Cl and O-Cl bondlengths are measured to be 2.25 Å and 1.82 Å, respectively. The passivation bondlengths with chlorine are found to be slightly contracted due to the edge interactions.

Along with the geometric properties, the nanoribbons are also investigated for their structural feasibility with E_b calculations. The E_b for the B-MgO-B is -5.35 eV. The negative E_b is an indication of the nanoribbons' structural feasibility. The B-MgO-B is found to have the most negative E_b indicating it is the most stable structure among the considered nanoribbons. The E_b is slightly reduced after passivation with chlorine at atleast one edge. The E_b of Cl-MgO-B and B-MgO-Cl are computed to be -5.27 eV and -5.12 eV. Cl-MgO-B is found to be relatively more stable compared to B-MgO-Cl. Since O and Cl are electronegative atoms, the repulsion forces between them could be the cause of reduced stability. The nanoribbon with chlorine passivation at both edges is found to have lowest stability with calculated E_b at -5.10 eV. It is interesting to note that the chlorine passivation slightly reduces the stability of the structures. The evaluated geometric parameters are tabulated in Table. 1.

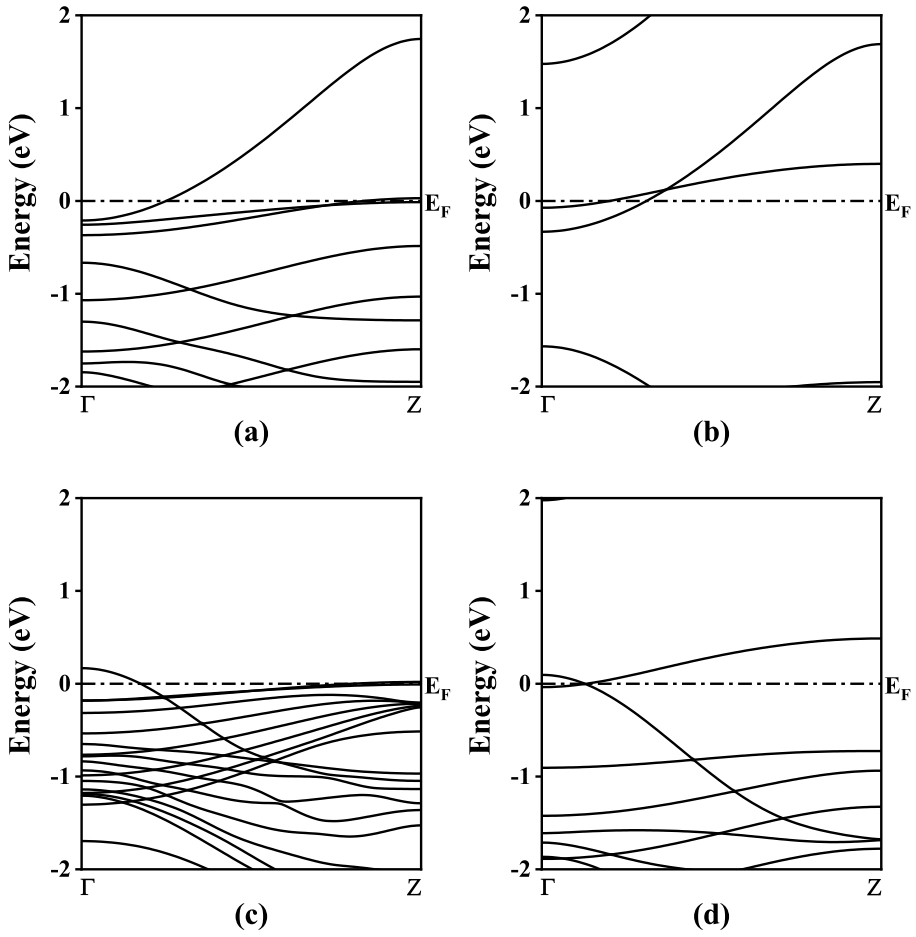


Figure 2. The computed MgONR bandstructures (a) B-MgO-B, (b) B-MgO-Cl, (c) Cl-MgO-B and (d) Cl-MgO-Cl. Fermi energy level is represented with dash dotted line at 0 eV.

Electronic properties

From the structural properties, it is clear that chlorine passivated MgONRs are structurally stable. Following the geometric analyses, we now investigate the electronic characteristics. To investigate the electronic properties, the bandstructure and desnity of states (DOS) calculations are performed and the results are depicted in Figure 2 and Figure 3, respectively. For the bare structure, the banstructure is shown in Fig. 2(a). From the bandstructure it is evident that B-MgO-B is metallic since the electronic energy states are cutting through the Fermi energy (E_F) level. Metallic nature of bare MgONRs is reported in previous works[28]. The energy states at the E_F are majorly contributed by the O-atoms at the O-edge. The energy states above 0 eV are majorly due to the Mg atoms at the Mg-edge while the energy states below 0 eV are due to the dominance of O-atoms at the O-edge. The overall bandstructure's energy states are dominated by the edge atoms. This indicates the significance of nanoribbon edges in the transport characteristics. For the B-MgO-Cl, the bandstructure changed due to chlorine passivation. The energy states in the valence band due to O-edge atoms seems to have been reduced due to chlorine passivation. The energy states close to the E_F are due to the O-Cl interactions. The electronic states farther from 0 eV in conduction band are due to the bare Mg-edge. However, for the Cl-MgO-B shown in Figure 2(c), the energy states in the conduction band close to E_F are due to the Mg-Cl interactions. However, the valence band states close to E_F are due to the bare O-edge atoms. The energy states far from E_F in the valence band are contributed by both the Mg-Cl atoms interactions and bare O-edge atoms. Finally for the Cl-MgO-Cl shown in Figure 2(d), The energy states in conduction band close to E_F are due to interaction between the O-atoms and the passivated chlorine atoms. In the valence band far from E_F, the energy states are due to Mg-Cl interactions.

Further, the DOS calculations are performed to validate the bandstructure results. The DOS plot of B-MgO-B is shown in Fig 3(a). The graph shows a non-zero DOS at E_F indicating the metallic nature of the nanoribbons. The energy states are denser in the valence band which is consistent with the higher electronic states in bandstructure reported in Figure 2(a). For the

Strcuture	Edge Mg-O Bondlengths (Å)		Mg-Cl (Å)	O-Cl (Å)	E_b (eV)	E_F (eV)
	Mg-Edge	O-edge				
B-MgO-B	1.88	1.86	–	–	-5.35	-3.83
Cl-MgO-B	1.90	1.86	2.28	–	-5.27	-5.60
B-MgO-Cl	1.90	1.87	–	1.88	-5.12	-2.70
Cl-MgO-Cl	1.92	1.88	2.25	1.82	-5.10	-4.03

Table 1. Computed bondlengths, E_b and E_F of the considered MgONRs

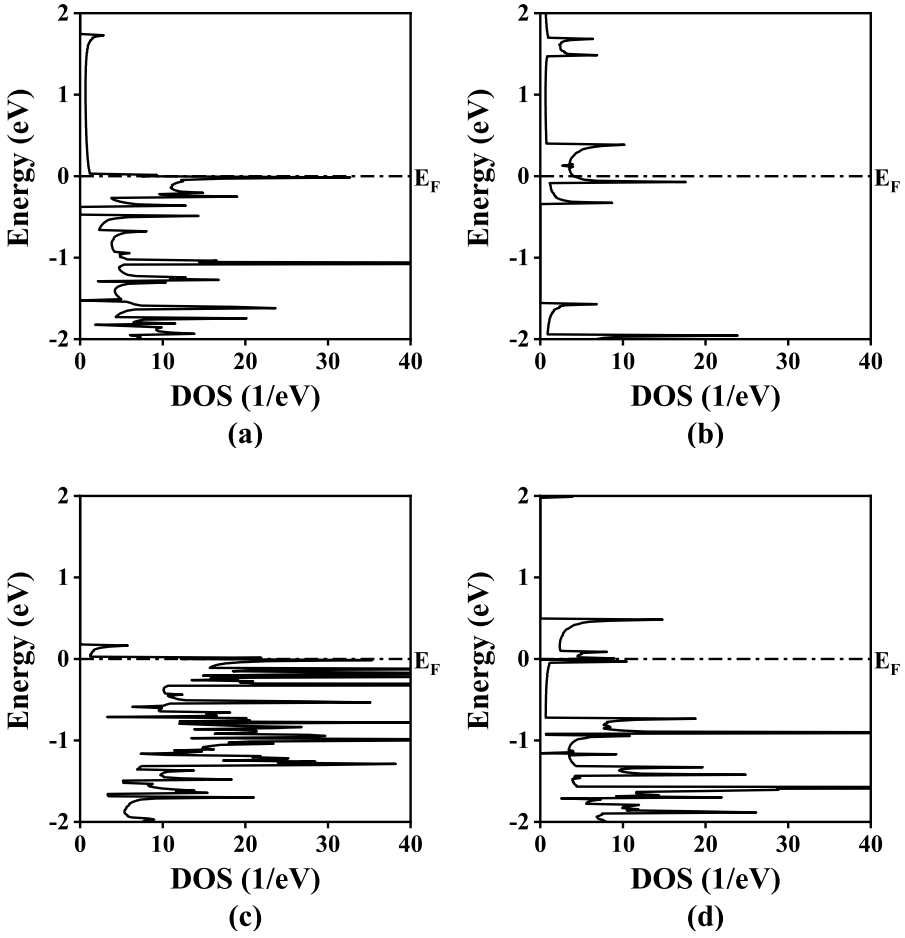


Figure 3. The computed MgONR DOS plots (a) B-MgO-B, (b) B-MgO-Cl, (c) Cl-MgO-B and (d) Cl-MgO-Cl. Fermi energy level is represented with dash dotted line at 0 eV.

B-MgO-Cl the energy states are close to the E_F while the DOS is reduced after -0.4 eV due to Cl passivation. The DOS is slightly increased in the conduction band close to E_F due to O-Cl bonding. For the Cl-MgO-B, the density of energy states is increased in the valence band which is similar to the result reported in bandstructure of Figure 2(c). The density of states in the conduction band is reduced for Cl-MgO-B. For the Cl-MgO-Cl in Fig. 3(d), the electronic states density is higher close to E_F due to the interactions with the chlorine atoms. The Mg-Cl interactions result in increased DOS close to the E_F in conduction band for B-MgO-Cl and far from E_F in valence band for Cl-MgO-B. From the bandstructure and DOS calculations it can be noted that all the structures retain their metallic nature. Further, the E_F of the MgONRs is evaluated. The E_F of B-MgO-B is located at -3.83 eV. When Cl is passivated at the O-edge, the E_F is upshifted to -2.70 eV indicating n-type behavior. Further,

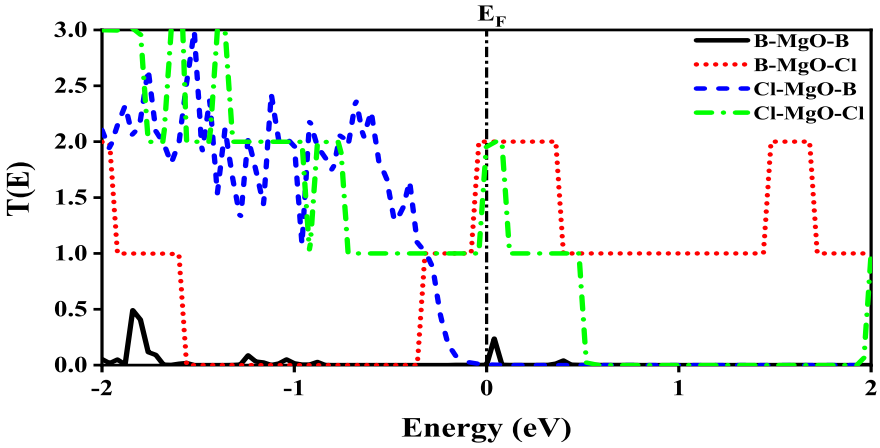


Figure 4. Zero bias transmission spectrum plots of MgONRs.

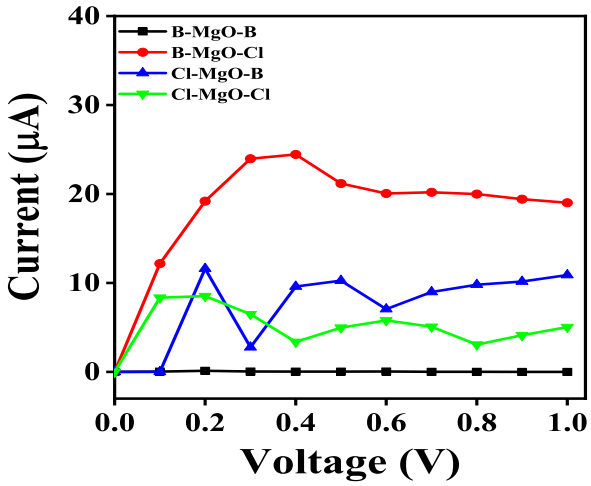


Figure 5. $V-I$ characteristics of considered MgONR devices.

when the Cl is passivated at Mg edge, the E_F is downshifted to -5.609 eV which shows a dominant p-type behavior. When Cl is passivated at both edges, the p-type behavior is noticed to be dominant. Further, the structures are examined for their transport characteristics in the following subsections.

Transport properties

The considered structures are now investigated for their transport properties using the two-probe method. The two-probe device configuration of the considered MgONR structures are shown in Figure 1. The method employs a central MgO area between the electrodes attached on either sides with periodic conditions. The zero bias transmission spectrum for the considered structures are shown in Figure 4. All the structures have a non-zero transmission peak at 0 eV which is due to their metallic nature. This explains the availability of electronic channels at the E_F for carrier transport. The obtained voltage-current ($V-I$) characteristics are depicted in Figure 5. From figure, it can be seen, that the current magnitude of bare structure is significantly less compared to chlorine passivated MgONRs. For the MgONRs with chlorine passivation, the current magnitude is significantly enhanced. Further, the chlorine passivated structures demonstrate an interesting NDR phenomenon between 0.4 V to 1.0 V for B-MgO-Cl and 0.2 V to 0.3 V for Cl-MgO-B, and 0.2-0.4 V for Cl-MgO-Cl. For the B-MgO-Cl, the current increases to 24.45 μA at 0.4 V and decreases to 19.01 μA at 1.0 V, whereas for the Cl-MgO-B, the current is at its peak when 0.2 V voltage is applied with a magnitude of 11.60 μA. Further increasing the voltage to 0.3 V, the current decreased to 2.76 μA. Similarly, the Cl-MgO-Cl device also exhibits NDR phenomenon between 0.2 V and 0.4 V. The current reaches a peak value of 8.52 μA at 0.2 V and then decreases to 3.37 μA at 0.4 V.

To have much more clearer understanding of the NDR characteristics, the bias dependent transmission spectrums of the considered structures are evaluated. The transmission spectrums are evaluated at the peak voltage and the valley voltage. For

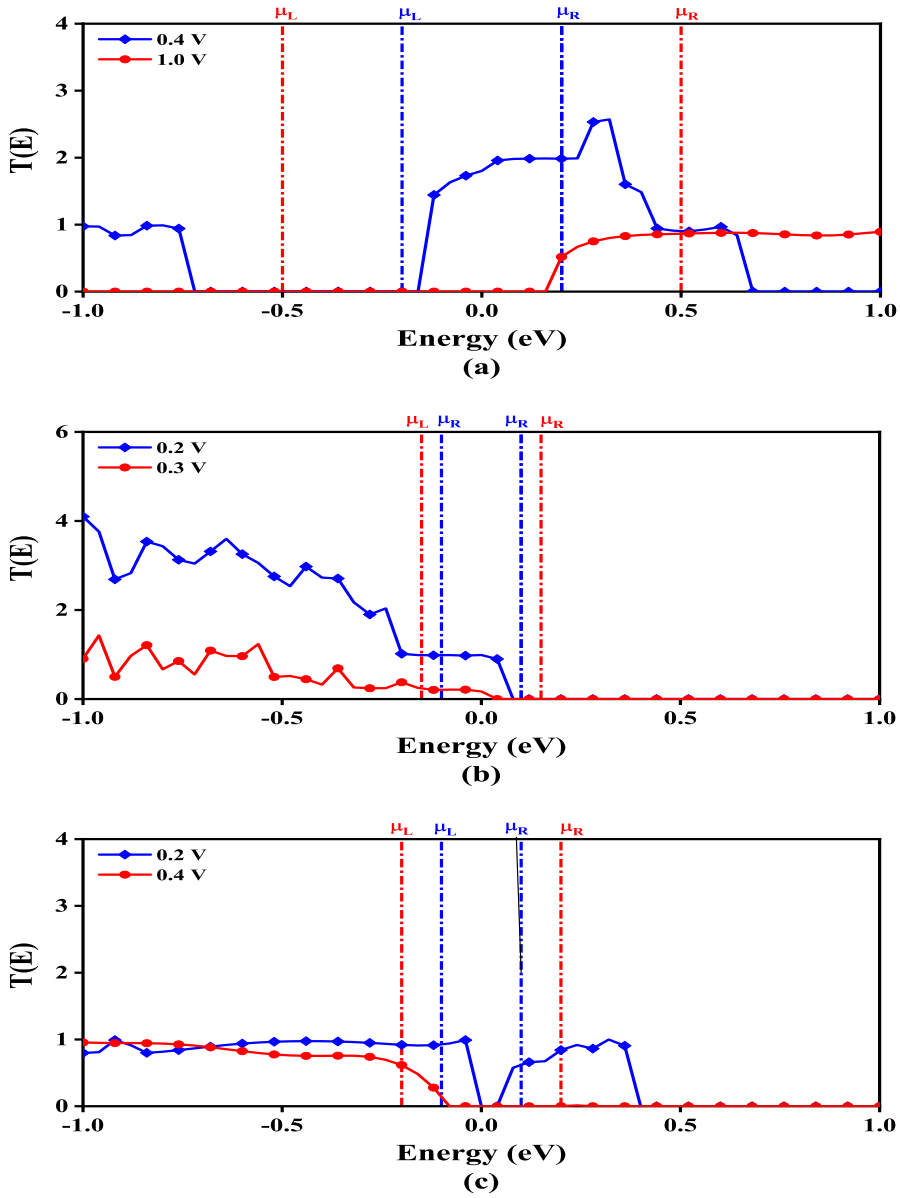


Figure 6. Bias dependent transmission spectrum plots of the chlorinated MgONRs (a) B-MgO-Cl, (b) Cl-MgO-B and (c) Cl-MgO-Cl.

the B-MgO-Cl device, the transmission spectrum is depicted in Fig. 6(a). As can be observed from figure, when a voltage of 0.4 V is applied, a huge transmission area can be observed between the electrode chemical potentials ($\mu_{L/R}$). For an applied bias of V_b the electrode potentials lie at $\pm eV_b/2$ The greater the transmission area between the electrode chemical potentials, the greater is the probability of transmission of carriers. This is evident from the huge magnitude of current for the B-MgO-Cl at 0.4 V. As the voltage is slightly increased to 1.0 V, the transmission area between the electrodes' chemical potentials is slightly reduced. This is reflected from the reduced current magnitude for the B-MgO-Cl at 1.0 V. A similar analysis is conducted for the Cl-MgO-B nanoribbon. As the device is applied with 0.2 V potential, a significant current mangnitude is noticed in the $V-I$ characteristics. As the potential is increased to 0.3 V, the a reduction in transmission area can be noticed which is reflected in the $V-I$ characteristics of Cl-MgO-B. A similar investigation is shown for Cl-MgO-Cl in Figure 6(c). At an applied potential voltage of 0.2 V a considerable transmission spectrum can be noticed between $\pm$ 0.1 eV. As the voltage is increased to 0.4 V, the transmission area is reduced which is in accordance with the reduced current magnitude reported in Figure 5. To further investigate the distribution energy states for NDR phenomenon we have evaluated the local device density of states (LDOS).

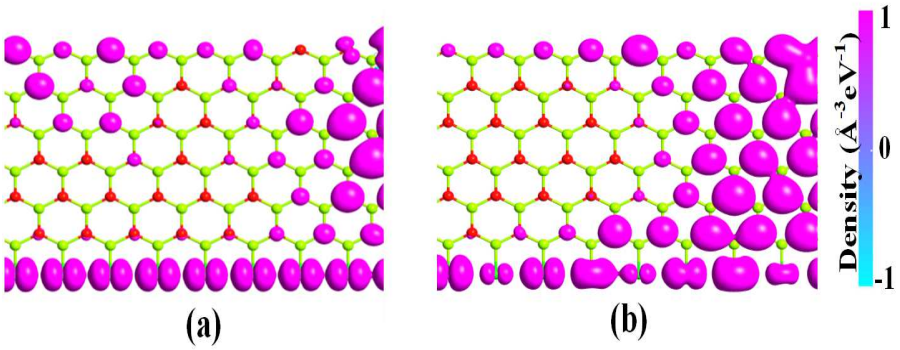


Figure 7. LDOS plots of Cl-MgO-B at (a) 0.2 V and (b) 0.3 V.

The LDOS plots of Cl-MgO-B device is evaluated and shown in Fig. 7 at 0.2 V (Figure 7(a)) and 0.3 V(Figure 7(b)). As can be seen in the figure, when a volatge of 0.2 V is applied, density of energy states is uniformly distributed from left electrode to right electrode. This increases the probability of carrier transport and the same can be seen with high current magnitude at 0.2 V for Cl-MgO-B in $V-I$ behavior. When the voltage is increased to 0.3 V, the delocalisation of electronic states density from left electrode to right electrode is reduced which causes the reduction in the carrier transport. Moreover, from the figure, it can be observed, that the carrier transport is majorly supported by the chlorine passivated edge of the nanoribbon.

The NDR peak-to-valley current ratio (PVCR) is the figure of merit for the NDR characteristics. The PVCR is computed by taking the peak or maximum magnitude of current over its next valley current or lowest magnitude of current. The computed PVCR for the B-MgO-Cl is found to be at 1.28. For the Cl-MgO-B, the PVCR is slightly increased to 4.19. For Cl-MgO-Cl, the PVCR is reduced to 2.28. The obtained PVCR of Cl-MgO-B is higher than silicene nanoribbons, bare boron nitride nanoribbons, selectively hydrogenated ZnO nanoribbons as reported in earlier research[32,35,43]. Owing to their meritorious properties, 2D materials are significant candidates for future nanoelectronic applications. In addition, semiconducting metal oxides offer faster response, higher sensitivities, simpler fabrication, and economic sensor design. In this context, the current chlorine passivated MgONRs provides provide interesting NDR characteristics that can be deployed in steep switching devices, oscillator design, resonant tunnel devices etc.[44] Although the PVCR is not significant enough, it could still serve as a starting step to explore the MgONRs for future nanoelectronic applications.

Conclusion

The current work presents the first principles investigation of chlorine passivated MgONRs for potential nanoelectronics applications. The chlorine atoms are selectively passivated at the egdes of the MgONRs. The structural investigations reveal the MgONRs are stable and the stability is relatively reduced when chlorine atoms are passivated at the edges. Additionally, electronic properties investigation reveals the metallic nature for the B-MgO-B nanoribbons. The metallic nature is retained despite passivation with chlorine atoms. The $V-I$ results obtained through the two-probe method reveal a considerable enhancement in the current mangitude of MgONRs upon chlorine passivation. Furthermonre, NDR pehnomenon is noticed in the chlorine passivated MgONRs. The NDR pehnomenon varies based on the type of chlorine passivation. The Cl-MgO-B nanoribbon exhibits a very high NDR PVCR of 4.19 under 0.5 V. The obtained findings suggest the considered chlorine passivated MgONRs can be used as promising candidates for future low power nanoelectronic steep switching devices, oscillators, resonant tunnel diodes etc.

Acknowledgements

We are thankful to Vellore Institute of Technology Chennai for providing us the computational resources.

Author contributions statement

Javvadi Sambasivarao has done the computational analysis, manuscript drafting, result analysis and graphical plotting. Aruru Sai Kumar contributed by literature review, images, reviewing and editing of manuscript.

Additional information

Corresponding authors: Aruru Sai Kumar

Competing interests

The authors of the manuscript do not have any competing interests.

Funding Declaration

The authors have no relevant financial or non-financial interests to disclose.

Data availability

The datasets used and/or analysed during the current study available from the corresponding author on reasonable request.

References

1. Plummer, J. D. & Griffin, P. B. Material and process limits in silicon vlsi technology. *Proc. IEEE.* **89**, 240–258 (2001).
2. Ito, T. & Okazaki, S. Pushing the limits of lithography. *Nature* **406**, 1027–1031 (2000).
3. Auth, C. *et al.* A 10nm high performance and low-power CMOS technology featuring 3^{rd} generation FinFET transistors, Self-Aligned Quad Patterning, contact over active gate and cobalt local interconnects. In *2017 IEEE International Electron Devices Meeting (IEDM)*, 29–1 (IEEE, 2017).
4. Chhowalla, M., Jena, D. & Zhang, H. Two-dimensional semiconductors for transistors. *Nat. Rev. Mater.* **1**, 16052 (2016).
5. Celler, G. K. & Cristoloveanu, S. Frontiers of silicon-on-insulator. *J. Appl. Phys.* **93**, 4955–4978 (2003).
6. Krivokapic, Z. *et al.* 14nm ferroelectric FinFET technology with steep subthreshold slope for ultra low power applications. In *2017 IEEE International Electron Devices Meeting (IEDM)*, 15–1 (IEEE, 2017).
7. Loubet, N. *et al.* Stacked nanosheet gate-all-around transistor to enable scaling beyond FinFET. In *2017 symposium on VLSI technology*, T230–T231 (IEEE, 2017).
8. He, X. *et al.* Impact of aggressive fin width scaling on FinFET device characteristics. In *2017 IEEE International Electron Devices Meeting (IEDM)*, 20–2 (IEEE, 2017).
9. Zhou, K. *et al.* Emerging 2D metal oxides: from synthesis to device integration. *Adv. Mater.* **35** (2023). Art. no. 2207774.
10. Liu, Y. *et al.* Promises and prospects of two-dimensional transistors. *Nature* **591**, 43–53 (2021).
11. Baig, N. Two-dimensional nanomaterials: A critical review of recent progress, properties, applications, and future directions. *Compos. - A: Appl. Sci. Manuf.* **165** (2023). Art. no. 107362.
12. Ansari, H. R., Nizamuddin, M., Manzoor, S. & Mishra, P. Performance analysis of doped zigzag graphene nanoribbon-based device for practical electronic applications using first principle approach. *Comput. Mater. Sci.* **247** (2025). Art. no. 113464.
13. Zhao, M., Casiraghi, C. & Parvez, K. Electrochemical exfoliation of 2D materials beyond graphene. *Chem. Soc. Rev.* **53**, 3036–3064 (2024).
14. Novoselov, K. S., Mishchenko, A., Carvalho, A. & Castro Neto, A. 2D materials and van der Waals heterostructures. *Science* **353** (2016). Art. no. aac9439.
15. Manzeli, S., Ovchinnikov, D., Pasquier, D., Yazyev, O. V. & Kis, A. 2D transition metal dichalcogenides. *Nat. Rev. Mater.* **2** (2017). Art. no. 17033.
16. Feng, J. *et al.* Synthesis of high surface area, mesoporous MgO nanosheets with excellent adsorption capability for Ni (II) via a distillation treating. *J. Colloid Interface Sci.* **438**, 259–267 (2015).
17. Choudary, B. M., Ranganath, K. V., Pal, U., Kantam, M. L. & Sreedhar, B. Nanocrystalline MgO for asymmetric Henry and Michael reactions. *J. Am. Chem. Soc.* **127**, 13167–13171 (2005).
18. Selvamani, T., Sinhamahapatra, A., Bhattacharjya, D. & Mukhopadhyay, I. Rectangular MgO microsheets with strong catalytic activity. *Mater. Chem. Phys.* **129**, 853–861 (2011).
19. Asl, M. A., Benam, M. R., Shahri, R. P., Feyzi, A. & Kafi, F. Two-dimensional quantum confinement effects on thermoelectric properties of MgO monolayers: A first principle study. *Micro Nanostructures* **163** (2022). Art. no. 107134.
20. Jin, C., Kim, H., Park, S. & Lee, C. Synthesis of biaxial MgO/Mg–Sn–O nanowire heterostructures and their structural and luminescence properties. *J. Alloy. Compd.* **541**, 163–167 (2012).

21. Matsuzaki, K., Hosono, H. & Susaki, T. Layer-by-layer epitaxial growth of polar MgO (111) thin films. *Phys. Rev. B, Condens. Matter Mater. Phys.* **82** (2010). Art. no. 033408.

22. Wang, F., Ta, N. & Shen, W. MgO nanosheets, nanodisks, and nanofibers for the Meerwein–Ponndorf–Verley reaction. *Appl. Catal. A: Gen.* **475**, 76–81 (2014).

23. Sun, L., He, H., Liu, C. & Ye, Z. Local super-saturation dependent synthesis of MgO nanosheets. *Appl. Surf. Sci.* **257**, 3607–3611 (2011).

24. Goniakowski, J., Noguera, C. & Giordano, L. Using Polarity for Engineering Oxide Nanostructures: Structural Phase Diagram in Free and Supported MgO (111) Ultrathin Films. *Phys. Rev. Lett.* **93** (2004). Art. no. 215702.

25. Kiguchi, M., Entani, S., Saiki, K., Goto, T. & Koma, A. Atomic and electronic structure of an unreconstructed polar MgO (111) thin film on Ag (111). *Phys. Rev. B* **68** (2003). Art. no. 115402.

26. Nilius, N. *et al.* Electronic and electrostatic properties of polar oxide nanostructures: MgO (111) islands on Au (111). *Phys. Rev. B: Condens. Matter Mater. Phys.* **86** (2012). Art. no. 205410.

27. He, J. *et al.* Magnetic properties of single transition-metal atom absorbed graphdiyne and graphyne sheet from DFT+ U calculations. *J. Phys. Chem. C* **116**, 26313–26321 (2012).

28. Krishna, M. S., Singh, S. & Kaushik, B. K. Edge tailored MgO nanoribbon for negative differential resistance/nanointerconnect applications. *Comput. Mater. Sci.* **231** (2024). Art. no. 112570.

29. Kang, S.-y., Kuang, F.-g., Huang, W., Zhang, C.-z. & Xu, Y.-q. Influence of hydrogen passivation, vacancies, and dopants on the electronic and magnetic properties of MgO nanoribbons. *Appl. Phys. A* **130** (2024). Art. no. 609.

30. Krishna, M. S., Kumar, A. S., Kankanala, S. & Nayak, A. K. First principles investigation of arsenic functionalized MgO nanoribbons. *Sci. Rep.* **16** (2026). Art. no. 10017.

31. Murugan, B. & Lee, S. Y. Two-dimensional materials based on negative differential transconductance and negative differential resistance for the application of multi-valued logic circuit: A review. *Carbon Lett.* **33**, 59–76 (2023).

32. Singh, S., De Sarkar, A., Singh, B. & Kaur, I. Electronic and transport behavior of doped armchair silicene nanoribbons exhibiting negative differential resistance and its fet performance. *RSC advances* **7**, 12783–12792 (2017).

33. Zhou, Y., Zhang, D., Zhang, J., Ye, C. & Miao, X. Negative differential resistance behavior in phosphorus-doped armchair graphene nanoribbon junctions. *J. Appl. Phys.* **115** (2014).

34. Zoghi, M. & Goharrizi, A. Y. Strain-induced armchair graphene nanoribbon resonant-tunneling diodes. *IEEE Transactions on Electron Devices* **64**, 4322–4326 (2017).

35. Kharwar, S., Singh, S. & Jaiswal, N. K. First-principle investigations of negative differential resistance in zigzag boron nitride nanoribbons. *Phys. E: Low-Dimens. Syst. Nanostructures* **134** (2021). Art. no. 114861.

36. Srivastava, P. K. *et al.* Resonant tunnelling diodes based on twisted black phosphorus homostructures. *Nat. Electron.* **4**, 269–276 (2021).

37. Krishna, M. S. & Singh, S. Selective edge hydrogenated armchair ZnO nanoribbons for negative differential resistance based nanoelectronic devices. *Phys. E: Low-Dimens. Syst. Nanostructures* **147** (2023). Art. no. 115570.

38. Taylor, J., Guo, H. & Wang, J. Ab initio modeling of quantum transport properties of molecular electronic devices. *Phys. Rev. B* **63** (2001). Art. no. 245407.

39. Brandbyge, M., Mozos, J.-L., Ordejón, P., Taylor, J. & Stokbro, K. Density-functional method for nonequilibrium electron transport. *Phys. Rev. B* **65** (2002). Art. no. 165401.

40. Tit, N., Othman, W., Shaheen, A. & Ali, M. High selectivity of N-doped ZnO nano-ribbons in detecting H_2, O_2 and CO_2 molecules: Effect of negative-differential resistance on gas-sensing. *Sens. Actuators B: Chem.* **270**, 167–178 (2018).

41. Perdew, J. P., Burke, K. & Ernzerhof, M. Generalized gradient approximation made simple. *Phys. Rev. Lett.* **77** (1996). Art. no. 3865.

42. Inge, S. V., Jaiswal, N. K. & Kondekar, P. N. Realizing negative differential resistance/switching phenomena in zigzag GaN nanoribbons by edge fluorination: A DFT investigation. *Adv. Mater. Interfaces* **4** (2017). Art. no. 1700400.

43. Krishna, M. S., Singh, S. & Kaushik, B. K. Planar quasi-1D nano-interconnects based on selective edge passivated ZnO nanoribbons. *IEEE Trans. Nanotechnol.* **22**, 597–605 (2023).

44. Shaheen, A., Othman, W., Ali, M. & Tit, N. Catalyst-induced gas-sensing selectivity in ZnO nanoribbons: Ab-initio investigation at room temperature. *Appl. Surf. Sci.* **505** (2020). Art. no. 144602.